

MEDICAL IMAGE FUSION USING ADAPTIVE BOX FILTERING AND NS TRANSFORM

Dr.M.V.SRUTHI, Associate Professor
KVSRRIT,Kurnool

ABSTRACT: Medical imaging sensors, such as positron emission tomography and single-photon emission computed tomography, may provide rich information, but each has its inherent drawbacks. Multimodal medical image fusion sensor becomes an effective solution in this scenario. Medical imaging's main objective is to collect as much preponderant and complementary data from the source as possible into a single product that can play a critical role in medical diagnosis and clinical operations. For multimodal sensor medical images, a novel fusion approach is proposed in this paper based on local difference (LD) in the non-sampled domain. The original medical images are first decomposed in this method. Then an operator called LD, fuses the sub-band coefficients. The final fused image is reconstructed with all composite coefficients through the reverse non-subsampled schemes. The new method of fusion has been implemented in several clinical studies, and the results show that this approach is much more transparent and efficient than some of the state-of-the-art approaches, both in terms of subjective visual performance and objective test outcomes. The quality of the proposed method was also compared to that of two non-sampled methods, i.e., non-sampled contourlet transformation and non-sampled shearlet transformation.

Index Terms— Image fusion, local difference (LD), medical image, multimodal sensor fusion, non-subsampled domain.

I.INTRODUCTION

THE core idea of image fusion is to extract as much predominant and complementary information as possible from multiple source images of the same scene and then fuse it into one single composite, with many more prominent features and much more useful information. Image fusion has been widely used in many areas, including remote sensing[1],[2] and medical diagnosis[3]. Due to its critical role in disease diagnosis, radiation therapy and surgery, the need to develop medical imaging technology has attracted increased and worldwide attention. In its current status, the technology allows one to track his or her health condition easily, and progression of illness, if any, through medical images. Medical images convey information about cells, tissues, bones, or organs, or structures, but it may differ from model to model information. In other words, the practical applications of medical images generated by

various models are not the same following details. 1) X-ray and computed tomography (CT) are very adept at describing dense structures, such as bones and implants, but they cannot capture physiological changes. 2) The soft tissues can be better visualized in magnetic resonance imaging (MRI) images, than do in CT images. 3) MRI-T1 images offer information on anatomical structure of tissues, while MRI-T2 can depict normal and pathological tissues [4]. 4) Positron emission tomography can display the metabolism of biological molecules, receptors, and neurotransmitters, in vivo, which is very helpful for cancer diagnosis. 5) Single-photon emission computed tomography (SPECT) differs from PET mainly in respect of image quality and the scope of applications. The image quality of PET is generally better than that of SPECT.

However, as the number of the tracer types of SPECT is much greater than that of PET, SPECT has a broader range of applications. From the foregoing observations, two important points emerge. First, the imaging principles of the above medical models vary significantly, because of which their applications also vary. Second, the medical image generated by a single modal commonly suffers from inadequate information, and hence it becomes necessary to fuse multimodal images to obtain much more accurate and comprehensive information. Obviously, the fusion of multimodal medical images helps not only in enhancing the precision of disease detection and diagnosis, but also in reducing the storage cost of patient's database, because only one composite image has to be stored, instead of multiple ones. According to the fusion principles, the existing image fusion methods can be divided broadly into two categories, namely, spatial domain-based methods and transform domain-based methods. The former is generally based on the arithmetic operations of the coefficients from different source images.

In other words, several weight values are given to each image in advance. In spite of its simplicity, this method often leads to side effects, such as contrast reduction and blurred details. The transform domain-based method adopts a different operating mechanism, which involves decomposition of the source images into a series of low-frequency and highfrequency subimages, with different scales and directions. Then, the subimages are fused to obtain the final image, following certain fusion rules.

So far, transform domain-based methods have been playing a dominant role in the field of image fusion. Du et al. [5] adopted the scheme of union Laplacian pyramid with multiple features to fuse medical images. Shen et al. [6] proposed cross-scale coefficient selection for volumetric medical image fusion. While discrete wavelet transform (DWT) is regarded as an ideal fusion scheme, Cheng et al. [7] utilized DWT for remote sensing image fusion. However, based on further research findings, it is argued that DWT can merely capture the point-wise information along finite directions. What is worse, DWT lacks shift invariance, due to downsampling. To overcome the limitations of DWT, several improved versions were presented, such as undecimated wavelet transform [8], [9], three-channel nonseparable symmetric wavelets [10], discrete fractional wavelet [11], and daubechies complex wavelet [12]. Zhou et al. [13] proposed a fusion scheme, based on multiscale weighted gradient. Srivastava et al. [14] integrate local energy with curvelet transform for the fusion of medical images.

The core idea of this proposal is to generate multimodal source medical images, using non-subsampled models, followed by fusion of low-frequency and high-frequency subimages. As LD can capture and provide good contrast between pixels, one can easily detect whether the pixel is from the clear region or not. The efficacy and superiority of the proposed framework were verified via a series of fusion experiments on multimodal medical data sets. The experimental results show that the performance of the proposed scheme is comparable with that of the current conventional fusion methods, in terms of both visual and quantitative performance. The following are the salient contributions of this paper. 1) A novel fusion framework, which relies on the nonsubsampling scheme, is proposed for obtaining multimodal sensor medical images. 2) LD is presented and used to complete fusion of low-frequency and high-frequency subimages. 3) Two different typical non-subsampled models, namely, NSCT and NSST, were considered for this paper. Discussions and comparisons were made with the experimental results. 4) Further, the proposed scheme was extended to perform multispectral fusion of multimodal medical images, such as SPECT-TI/MRI and SPECT-Tc/MRI images. Experimental results demonstrate that the proposed scheme can rectify and improve image information, which in turn enhances the precision of disease detection and diagnosis.

II. DISTRIBUTION CHARACTERISTICS OF BRIGHTNESS AND COLOR

To detect and capture the valuable pixel from a medical image is always a challenging task in health care, because even a minor point may offer a vital clue for patient's treatment. In fact, human visual system is very sensitive to the contrast in the brightness of the image, which broadly reflects the real quality of the image. This inspired the authors to conduct several simulation experiments to obtain statistical data on the potential relationship between certain indexes and the image quality. It was found that brightness and color (colored images) distribution of the pixel is closely related to the amount of information it contains. Specifically, if the source images are gray, the brightness distribution of salient regions (most likely the lesion) is commonly different from that of other regions. On the other hand, if the source images are colored, the distributions of both brightness and color are prominent. Fig. 1 depicts two multimodal images of a brain glioma case, which were downloaded from the Harvard University site (<http://www.med.harvard.edu/AANLIB/home.htm>).

The MR-T2 image shown in Fig. 1(b) demonstrates an area of mixed signal intensity on proton density (PD) and T2-weighted (T2) images in the left occipital region. Contrast enhancement shows cystic elements in the lesion. Thallium (SPECT-TI) image, shown in Fig. 1(e), depicts an anterior border of high uptake, consistent with a small region of tumor recurrence [30]. Two different regions, each containing 16×28 pixels, were chosen from Fig. 1(b) and (e). As the two pairs are from different regions, the comparisons of their mean brightness and color are illustrated in Fig. 2. The greater the color component (such as bright red and bright green), the larger is the saturation degree. On the contrary, the saturation is inversely proportional to the achromatic component. Interestingly, it can be concluded that the intensities of brightness and color of pixels are prone to vary largely from region to region. Obviously, the lesion regions, marked as Fig. 1(c) and (f), contain much more information than the normal sites. This leads to the question whether the result in Fig. 2 is a mere coincidence or a reflection of some inherent reasons behind it? Considering the SPECT image, for example, the imaging principle of SPECT is based mainly on the tracer molecules entering the human circulatory system, which can reflect the difference in the tissue intensity, based on the component concentrations in different tissues. The cancer cells of the tumor are generally much more active than normal ones, and hence the region corresponding to cancer cells is usually of a much darker color (bright red and yellow), as can be seen from Fig. 1(e). Based

on the interesting phenomenon mentioned above, it was attempted in this paper to detect and locate the pixels of the lesion as precisely as possible.

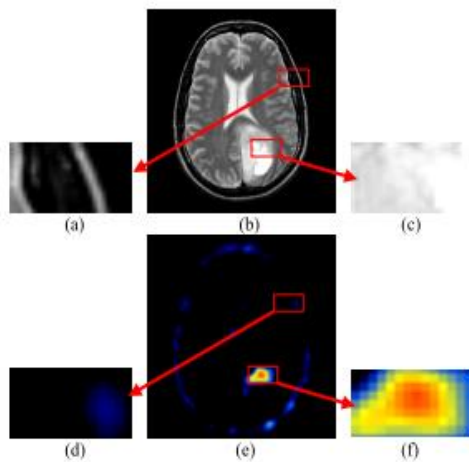


Fig. 1. Brightness and color distributions of T2-weighted image and SPECT-TI image. (a) Enlarged subimage II of (b). (b) T2 weighted image. (c) Enlarged subimage II of (b). (d) Enlarged subimage II of (e). (e) SPECT-TI image. (f) Enlarged subimage II of (e).

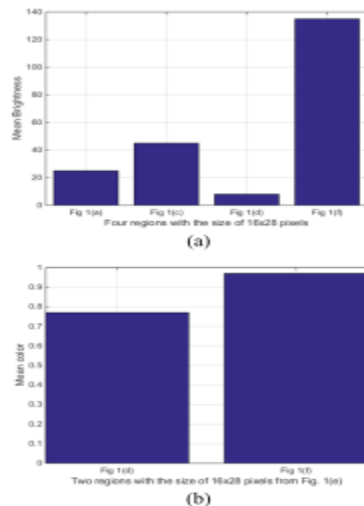


Fig. 2. Comparisons of mean brightness and color. (a) Comparisons of mean brightness. (b) Comparisons of mean color.

III. PROPOSED MULTIMODAL MEDICAL IMAGE FUSION FRAMEWORK

There are three sections in this chapter. The LD system is included in Section III-A. Section III-B explains the multimodal clinical image fusion system. Section III-C extends the process of fusion to process color images.

A. Local Difference

Compared to the pixel's own numerical value, people are more concerned about the brightness rate comparison. In other words, the pixel whose intensity level differs from that of the neighboring pixels is more likely to be of greater interest, as it may be located at some important edge or region boundary. Coincidentally, the non-sampled models' objective is to screen the main and detailed information. The non-sampled method, as already stated, can be used to distinguish low-frequency components from high-frequency components. The former is responsible for characterizing the key contours of the source image, while the latter emphasizes the presentation of detailed information, such as edges and boundaries of regions. The average and max absolute-based rules are usually followed in traditional fusion frameworks to complete the fusion process. The former method, however, also leads to a reduction in the contrast of the final fused image, whereas the latter approach leads to the inclusion of noisy points in the final fused image due to its sensitivity to noise, although the pixel with greater absolute values often belongs to the salient characteristics. What is worse, the max absolute scheme takes into account only the single pixel, rather than the local region. Single pixels are obviously not enough to determine the exact location of the lesion. To weigh and determine the information of the pixel more reasonably and accurately, LD is proposed to fuse the subimages in this paper. Mathematically, LD is expressed as follows:

$$LD(i, j) = \begin{cases} \frac{SF(i, j)}{|L_N(i, j) - \alpha f(i, j)|}, & \text{if } L_N(i, j) \neq \alpha f(i, j) \\ & \&\& \text{if } (\alpha = 0), L_N(i, j) \neq 0 \\ SF(i, j), & \text{else} \end{cases} \quad (1)$$

where SF (spatial frequency) denotes the level difference between the pixel located at (i, j) and those surrounding it; LN describes the general feature of the region centered at (i, j); f (i, j) is the gray or saturation value; and α is a variable, which is determined by the coefficients of the subimage. The mathematical expression of SF is given as follows:

$$SF(x, y) = \sum_{x=i-(m-1)/2}^{i+(m-1)/2} \sum_{y=j-(n-1)/2}^{j+(n-1)/2} \frac{\partial^2 f(x, y)}{\partial x^2} + \frac{\partial^2 f(x, y)}{\partial y^2} \quad (2)$$

where the size of the neighborhood region is postulated as $m \times n$. Typically, the region is a square, i.e., $m = n$ and m is an odd number. Further, because

of the close distance between the pixel (i, j) and its four neighbors in the horizontal and vertical directions, (2) can be rewritten as

$$\begin{aligned}
 SF(x, y) &= \sum_{x=i-(m-1)/2}^{i+(m-1)/2} \sum_{y=j-(m-1)/2}^{j+(m-1)/2} \frac{\partial^2 f(x, y)}{\partial x^2} + \frac{\partial^2 f(x, y)}{\partial y^2} \\
 &= [f(x + (m - 1)/2, y) + f(x - (m - 1)/2, y) - 2f(x, y)] \\
 &\quad + [f(x, y + (m - 1)/2) + f(x, y - (m - 1)/2) - 2f(x, y)] \\
 &= |f(x + (m - 1)/2, y) - f(x, y)| \\
 &\quad + |f(x - (m - 1)/2, y) - f(x, y)| \\
 &\quad + |f(x, y + (m - 1)/2) - f(x, y)| \\
 &\quad + |f(x, y - (m - 1)/2) - f(x, y)|. \tag{3}
 \end{aligned}$$

As for LN , there are two different situations.

1) If all the coefficients of the subimage are nonnegative, LN stands for the average gray or color level of the region, centered at (i, j). In this case, α equals to 1. Obviously, the value $|LN - f(i, j)|$ reflects the extent of difference between the pixel itself and the region.

2) If there are some pixels with negative values, such as those of the high-frequency subimages, then α equals to 0. Here, LN denotes the average gray level of the local region, centered at (i, j) in the low-frequency subimage. In this situation, LD can be used to detect and capture the feature points.

B. Fusion Framework

This section presents in detail the steps involved in the proposed fusion framework. Suppose that there are two source medical images, called A and B, which have been properly registered. After non-subsampled decompositions, a pair of low-frequency subimages and a series of high-frequency subimages can be obtained, namely, $\{L_{A,k,d}, L_{B,k}\}$ and $\{H_{A,k,d}, H_{B,k,d}\}$. “H” and “L” denote high frequency and low frequency, respectively. “K” stands for the total decomposition level, while “k” and “d” represent, respectively, certain decomposition level and direction. Obviously, variable “k” must satisfy the condition $1 \leq k \leq K$. As both NSCT and NSST share the non-subsampled characteristic, they were abbreviated for simplicity as “NS” in the following fusion diagram. The steps involved in the proposed fusion framework are as follows.

1) A and B are decomposed via NS into a pair of low-frequency subimages $L_{A,K}$ and $L_{B,K}$, and a series of high-frequency subimages $H_{A,k,d}$ and $H_{B,k,d}$. “K” stands for total decomposition level. $H_{A,k,d}$ and $H_{B,k,d}$ represent the high-frequency subimages of A and B at level $k \in [1, K]$, and orientation d.

2) LD is used to complete the fusion of low-frequency and high-frequency subimages. The coefficients of the fused subimages follow the fusion rule given as follows:

$$F_{K(k,d)}(i, j) = \begin{cases} \chi_{A,K(k,d)}(i, j), & \text{if } LD_{A,K(k,d)}(i, j) \geq LD_{B,K(k,d)}(i, j) \\ \chi_{B,K(k,d)}(i, j), & \text{else} \end{cases} \tag{4}$$

where $F_{K(k,d)}$ stands for the fused subimage and χ stands for the low-frequency subimage “L” or the high-frequency subimage “H.” Here, the result of the operator LD is regarded as the only factor that needs to be taken into account to decide the coefficients of the subimages. 3) The final fused image F is reconstructed by using the inverse NS.

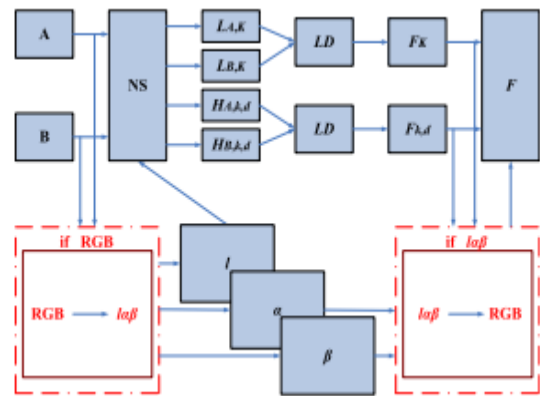


Fig. 3. Block diagram of the proposed fusion framework.

C. Color Image Fusion

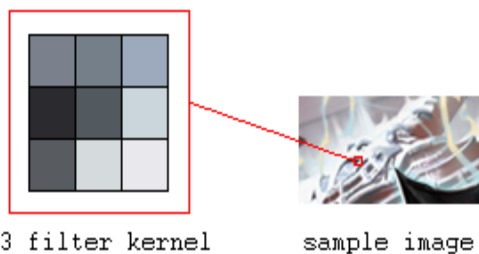
The color is usually characterized by three independent attributes, which mutually interact to form a spatial coordinate, called color space. The color space can be divided into two categories, namely, primary color space and color brightness separation color space, depending on its basic structure. RGB is the typical representative of primary color space and $\alpha\beta$, the color brightness separation color space [31]. RGB mode is an additive one with luminescent screen, while CMYK mode is a printing subtractive one with reflective color. IHS mode suffers from spectral information distortion, which easily leads to medical accidents. Unlike these three common modes, $\alpha\beta$ mode can deal with brightness or color without mutual influences, and so it does not depend on either light or pigment. Moreover, $\alpha\beta$ includes all color modes the humans can see in theory, and it can make up for the drawbacks of RGB, CMYK, and IHS. Therefore, $\alpha\beta$ mode was chosen as the color space for this paper. During the fusion of medical source images, one may

encounter color images, such as SPECT-TI- and SPECT-Tc-based ones, in which case, the RGB source image is first converted into the $\alpha\beta$ version, as shown in the lower left corner of Fig. 3, to obtain the three components, namely, α , β , and γ . α represents an achromatic channel, and β and γ represent the chromatic yellow-blue and red-green channels, respectively. These channels are symmetrical and compact. The α component is fused, using the proposed scheme, and then $\alpha\beta$ converted to RGB (see the lower right corner of Fig. 3) to get the final fused image F .

BOX FILTERING

Box filtering is basically an average-of-surrounding-pixel kind of image filtering. It is actually a convolution filter which is a commonly used mathematical operation for image filtering. A convolution filter provides a method of multiplying two arrays to produce a third one. In box filtering, *image sample* and the *filter kernel* are multiplied to get the *filtering result*. The filter kernel is like a description of how the filtering is going to happen, it actually defines the type of filtering. The power of box filtering is one can write a general image filter that can do sharpen, emboss, edge-detect, smooth, motion-blur, etcetera. Provided appropriate filter kernel is used.

Now that I probably had wet your appetite let us see further the coolness of box filtering and its filter kernel. A filter kernel defines filtering type, but what exactly is it? Think of it as a fixed size small box or window larger than a pixel. Imagine that it slides over the sample image through all positions. While doing so, it constantly calculates the average of what it sees through its window.



The minimum standard size of a filter kernel is 3x3, as shown in above diagram. Due to the rule that a filter kernel must fit within the boundary of sampling image, no filtering will be applied on all four sides of the image in question. With special treatment, it can be done, but what is more important than making the basic work first? Enough talk, lets get to the implementation asap!

A **box blur** (also known as a box linear filter) is a spatial domain linear filter in which each pixel in the resulting image has a value equal to the average value

of its neighboring pixels in the input image. It is a form of low-pass ("blurring") filter. A 3 by 3 box blur can be written as matrix

Due to its property of using equal weights, it can be implemented using a much simpler accumulation algorithm, which is significantly faster than using a sliding-window algorithm.^[1] Box blurs are frequently used to approximate a Gaussian blur.^[2] By the central limit theorem, repeated application of a box blur will approximate a Gaussian blur.

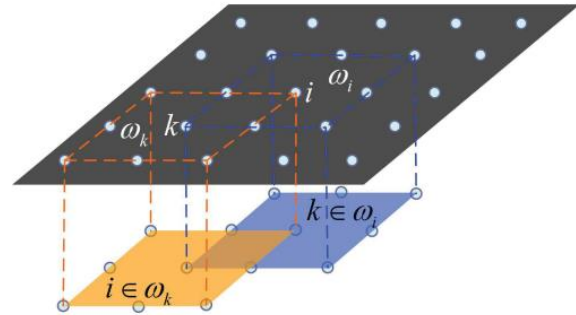


Fig4: window choice

IV. EXPERIMENTAL RESULTS

To demonstrate the effectiveness of the proposed scheme, eight pairs of human brain images, shown in Fig. 4, were considered. For simplicity, they were named as pairs I–VIII. The source images were of diverse origin and nature, as they were produced by different imaging sensors, such as CT, MRI, and SPECT; some of them are colored, while the others are not. Besides diversity, a few more points need to be specified here, regarding the images. 1) All the source images are of the same size, each containing 256×256 pixels. 2) The gray images, including those of CT and MRI, were of 256-level gray scale, while the color images, such as those of SPECT, were in pseudocolor. 3) All the source images were properly registered. 4) They can be accessed and downloaded from the Harvard university site (<http://www.med.harvard.edu/AANLIB/home.htm>). Because of the differences in imaging mechanism and environment, the images produced by different modals contain a lot of mutually complementary information. Therefore, it is expected that the fused image will offer much information for medical diagnosis and clinical operations. The effectiveness of the proposed fusion method was verified by comparing its performance with that of seven recently published methods, which are based on multiscale weighted gradient-based fusion (MWGF) [13], NSRCxWT [22], QPSO-PCNN [25], ASR [26], CSR [27], GFF [28], and CBF [29]. To ensure fairness in simulation experiments, the parameter settings of the above-cited seven techniques still follow the contents of the respective references. One

can get more information on these techniques by referring to related contents. As for the proposed schemes, namely, NSCT-LD and NSST-LD, the decomposition stages of both NSCT and NSST were set as 4 and the direction number from coarser to finer scales as (4, 8, 8, 16).

	ASR	QPSD-PCNS	CSR	NSRCS-WT	GFF	MWGF	CBF	NSCT-LD	NSST-LD		
Pair I	Q_{μ}	34.8118	36.0681	44.1029	42.4388	35.9596	42.1331	36.8943	44.5385	45.3108	56.37
	Q_{σ}	0.7094	0.7001	0.7219	0.7299	0.7224	0.7461	0.7302	0.7252	0.7449	0.9150
	Q_{μ}	0.7083	0.7799	0.8813	1.1378	0.6984	1.1624	0.7198	1.1632	1.1654	3.4516
	Q_{σ}	0.2387	0.3911	0.3491	0.6577	0.4083	0.7813	0.1445	0.7108	0.8347	1.1198
	QG	D	C+	C	B	D+	B	E+	B	A	
Pair II	Q_{μ}	40.8550	44.3366	50.9756	49.7400	39.9966	41.5393	47.7477	50.2457	51.4829	54.40
	Q_{σ}	0.7373	0.7431	0.6991	0.7465	0.6587	0.5034	0.7377	0.7513	0.7833	0.9280
	Q_{μ}	0.6974	0.8054	0.8798	1.0625	0.7074	1.0301	0.7735	1.0388	1.0122	2.1393
	Q_{σ}	0.4107	0.5017	0.3950	0.4138	0.5461	0.6789	0.3444	0.6249	0.6828	1.0539
	QG	D	B	C	C+	D	D+	D	B	B+	
Pair III	Q_{μ}	39.0054	40.5021	41.8544	40.3706	38.8861	42.1330	38.1430	42.4332	42.7165	54.09
	Q_{σ}	0.8974	0.8998	0.9014	0.9009	0.9053	0.9061	0.9012	0.9083	0.9102	0.9138
	Q_{μ}	0.9498	0.9977	1.0634	0.9922	0.9013	1.0120	0.8901	1.0788	1.2790	1.9315
	Q_{σ}	0.6989	0.6855	0.6306	0.6431	0.7626	0.7534	0.4382	0.7886	0.7763	1.326
	QG	C	C+	C	C+	B	B+	D	A	B+	
Pair IV	Q_{μ}	32.4983	33.7310	37.9965	38.2592	33.9784	36.4993	32.4219	38.8105	39.4472	54.47
	Q_{σ}	0.8349	0.8379	0.8244	0.8339	0.8346	0.8285	0.8355	0.8393	0.8426	0.9113
	Q_{μ}	0.8334	0.8719	1.0449	1.0640	0.8792	0.9869	0.8362	1.0851	1.2525	2.1817
	Q_{σ}	0.8749	0.5853	0.7152	0.7223	0.7631	0.7447	0.4054	0.7212	0.7493	1.7598
	QG	C	D+	C+	C	C	D+	E+	B	B+	

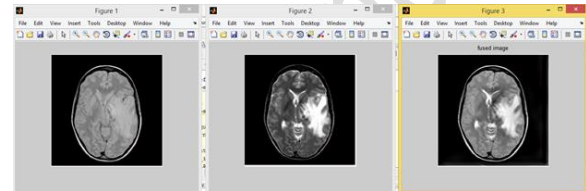
spatial frequency (QSF)
5.4409e+001 +3.5923e+002i

phase congruency (QP)
1.0539

mutual information (QMI)
2.1393

Piella's metric (QPiella)
0.9280

Pair 3



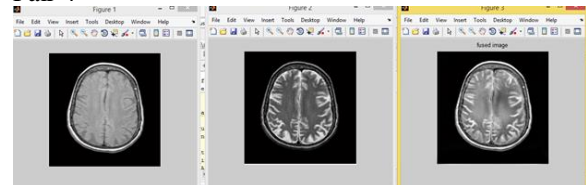
spatial frequency (QSF)
5.4097e+001 +3.5921e+002i

phase congruency (QP)
1.3326

mutual information (QMI)
1.9315

Piella's metric (QPiella)
0.9138

Pair 4



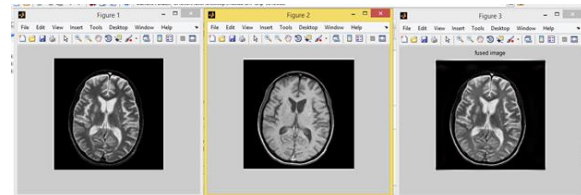
spatial frequency (QSF)
5.4473e+001 +3.0504e+002i

phase congruency (QP)
1.7598

mutual information (QMI)
2.1817

Piella's metric (QPiella)
0.9113

PAIR 1



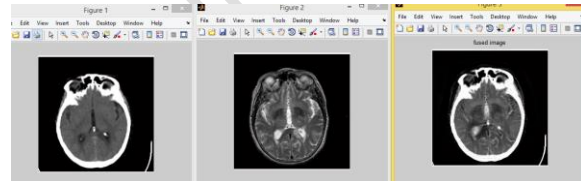
spatial frequency (QSF)
5.6377e+001 +3.5921e+002i

phase congruency (QP)
1.1198

mutual information (QMI)
3.4516

Piella's metric (QPiella)
0.9150

Pair-2



V. CONCLUSION

A novel fusion model for multimodal medical images of sensors is provided in this paper, based on LD in the non-sampled domain. For this paper, two conventional non-sampled models, namely NSCT and NSST, are considered and compared in comparison to the methodology in previous references. This paper's key contributions can be summarized as follows. 1) For multimodal sensor medical images, which relies on the non-sampled scheme, a novel fusion framework is proposed. A series of simulation tests were performed under ideal and extreme conditions, and the methods based on the proposed scheme were found to be surprisingly superior to the current traditional methods in terms of both visual performance and objective assessment outcomes. 2) LD was found to be the only index to signal the Completion of low-frequency and high-frequency sub-images fusion work. 3) Two typical non-sampled models were considered and compared, namely NSCT and NSST. 4) The proposed scheme has also been expanded to tackle multi-spectral fusion of multimodal clinical images, such as SPECT-TI / MRI and SPECT-Tc / MRI images. The researchers claim that the approach proposed has great potential to rectify and enhance image data, which in turn will increase the reliability of disease detection and diagnosis.

REFERENCES

[1] H. R. Shahdoosti and H. Ghassemian, "Combining the spectral PCA and spatial PCA fusion methods by an optimal filter," *Inf. Fusion*, vol. 27, pp. 150–160, Jan. 2016.

[2] H. R. Shahdoosti and N. Javaheri, "Pansharpening of clustered MS and Pan images considering mixed pixels," *IEEE Trans. Geosci. Remote. Lett.*, vol. 14, no. 6, pp. 826–830, Jun. 2017.

[3] H. R. Shahdoosti and A. Mehrabi, "MRI and PET image fusion using structure tensor and dual ripplet-II transform," *Multimedia Tools Appl.*, vol. 77, no. 17, pp. 22649–22670, 2018.

[4] Y. Yang, Y. Que, S. Huang, and P. Lin, "Multimodal sensor medical image fusion based on type-2 fuzzy logic in NSCT domain," *IEEE Sensors J.*, vol. 16, no. 10, pp. 3735–3745, May 2016.

[5] J. Du, W. Li, B. Xiao, and Q. Nawaz, "Union Laplacian pyramid with multiple features for medical image fusion," *Neurocomputing*, vol. 194, pp. 326–339, Jun. 2016.

[6] R. Shen, I. Cheng, and A. Basu, "Cross-scale coefficient selection for volumetric medical image fusion," *IEEE Trans. Biomed. Eng.*, vol. 60, no. 4, pp. 1069–1079, Apr. 2013.

[7] J. Cheng, H. Liu, T. Liu, F. Wang, and H. Li, "Remote sensing image fusion via wavelet transform and sparse representation," *ISPRS J. Photogramm. Remote Sens.*, vol. 104, pp. 158–173, Jun. 2015.

[8] E. Andreas, C. L. Pagliari, and E. A. B. da Silva, "Multiscale image fusion using the undecimated wavelet transform with spectral factorization and nonorthogonal filter banks," *IEEE Trans. Image Process.*, vol. 22, no. 3, pp. 1005–1017, Mar. 2013.

[9] P. R. Hill, N. Anantrasirichai, A. Achim, M. E. Al-Mualla, and D. R. Bull, "Undecimated dual-tree complex wavelet transforms," *Signal Process., Image Commun.*, vol. 35, no. 1, pp. 61–70, Jul. 2015.

[10] B. Liu, K. Li, W. Liu, and F. Liu, "Construction method of three-channel non-separable symmetric wavelets with arbitrary dilation matrices and its applications in multispectral image fusion," *IET Image Process.*, vol. 7, no. 7, pp. 679–685, Oct. 2013.

[11] X. Xu, Y. Wang, and S. Chen, "Medical image fusion using discrete fractional wavelet transform," *Biomed. Signal Process. Control*, vol. 27, pp. 103–111, May 2016.

[12] R. Singh and A. Khare, "Fusion of multimodal medical images using Daubechies complex wavelet transform—A multiresolution approach," *Inf. Fusion*, vol. 19, no. 9, pp. 49–60, 2014.

[13] Z. Zhou, S. Li, and B. Wang, "Multi-scale weighted gradient-based fusion for multi-focus images," *Inf. Fusion*, vol. 20, no. 1, pp. 60–72, 2014.

[14] R. Srivastava, O. Prakash, and A. Khare, "Local energy-based multimodal medical image fusion in curvelet domain," *IET Comput. Vis.*, vol. 10, no. 6, pp. 513–527, Sep. 2016.

[15] M. N. Do and M. Vetterli, "The contourlet transform: An efficient directional multiresolution image representation," *IEEE Trans. Image Process.*, vol. 14, no. 12, pp. 2091–2106, Dec. 2005.

[16] V. Bhateja, H. Patel, A. Krishn, A. Sahu, and A. Lay-Ekuakille, "Multimodal medical image sensor fusion framework using cascade of wavelet and contourlet transform domains," *IEEE Sensors J.*, vol. 15, no. 12, pp. 6783–6790, Dec. 2015.

[17] A. L. da Cunha, J. Zhou, and M. N. Do, "The non-sampled contourlet transform: Theory, design, and applications," *IEEE Trans. Image Process.*, vol. 15, no. 10, pp. 3089–3101, Oct. 2006.

[18] J. M. Murphy, J. Le. Moigne, and D. J. Harding, "Automatic image registration of multimodal remotely sensed data with global shearlet features," *IEEE Trans. Geosci. Remote Sens.*, vol. 54, no. 3, pp. 1685–1704, Mar. 2016.

[19] K. Azam, H. Rob, and P. Scheunders, "Band-specific shearlet-based hyperspectral image noise reduction," *IEEE Trans. Geosci. Remote.*, vol. 53, no. 9, pp. 5054–5066, Sep. 2015.

- [20] G. M. Sun, J. S. Leng, and T. Z. Huang, "An efficient sparse optimization algorithm for weighted 0 shearlet-based method for image deblurring," *IEEE Access*, vol. 5, pp. 3085–3094, 2017.
- [21] G. Easley, D. Labate, and W.-Q. Lim, "Sparse directional image representations using the discrete shearlet transform," *Appl. Comput. Harmon. Anal.*, vol. 25, no. 1, pp. 25–46, 2008.
- [22] S. S. Chavana, A. Mahajan, S. N. Talbar, S. Desai, M. Thakur, and A. D'Cruz, "Nonsampled rotated complex wavelet transform (NSRCxWT) for medical image fusion related to clinical aspects in neurocysticercosis," *Comput. Biol. Med.*, vol. 81, no. 2, pp. 64–78, 2017.
- [23] L. Wang, B. Li, and L.-F. Tian, "Multi-modal medical image fusion using the inter-scale and intra-scale dependencies between image shiftinvariant shearlet coefficients," *Inf. Fusion*, vol. 19, no. 9, pp. 20–28, 2014.
- [24] W. Zhao and H. Lu, "Medical image fusion and denoising with alternating sequential filter and adaptive fractional order total variation," *IEEE Trans. Instrum. Meas.*, vol. 66, no. 9, pp. 2283–2294, Sep. 2017.
- [25] X. Xu, D. Shan, G. Wang, and X. Jiang, "Multimodal medical image fusion using PCNN optimized by the QPSO algorithm," *Appl. Soft Comput.*, vol. 46, pp. 588–595, Sep. 2016.
- [26] Y. Liu and Z. Wang, "Simultaneous image fusion and denoising with adaptive sparse representation," *IET Image Process.*, vol. 9, no. 5, pp. 347–357, 2015.
- [27] Y. Liu, X. Chen, R. K. Ward, and Z. J. Wang, "Image fusion with convolutional sparse representation," *IEEE Signal Process. Lett.*, vol. 23, no. 12, pp. 1882–1886, Dec. 2016